Journal of
Manufacturing and Materials Processing

MDPI

Article

Assessment of Pinless Tools Efficiency in FSSW of Thick High-Strength Low-Alloy Steels for Structural Lap Joints

David Gomes Andrade [1], Sree Sabari [1], Carlos Leitão [2] and Dulce M. Rodrigues [3,*]

[1] ISISE, ARISE, Department of Civil Engineering, University of Coimbra, 3030-788 Coimbra, Portugal; david.andrade@uc.pt (D.G.A.); sree.sabari@uc.pt (S.S.)
[2] CEMMPRE, ARISE, Department of Mechanical Engineering, University of Coimbra, 3030-788 Coimbra, Portugal; carlos.leitao@dem.uc.pt
[3] ISISE, ARISE, Department of Mechanical Engineering, University of Coimbra, 3030-788 Coimbra, Portugal
* Correspondence: dulce.rodrigues@dem.uc.pt; Tel.: +351-239-797-219

Abstract

In this study, the maximum achievable weldable thickness in spot welding with pinless tools was investigated by welding multiple stacks of 1 mm thick high-strength steel HC420LA. This approach allowed for the evaluation of heat dissipation during the welding of progressively thicker sections, as well as for the comparison of the joints strength for increasing welded thicknesses. The methodology used also enabled the identification of the key technical challenges in achieving high-quality welds using very short welding times. Notably, even for a 5 s weld, a four-sheet configuration (4 mm thickness) was successfully joined, achieving a maximum shear load of approximately 10 kN and exhibiting a refined acicular ferritic bainitic microstructure with metallic continuity across the steel interfaces. The highest mechanical performance was obtained in the welds produced within 30 s, which reached a maximum shear load of approximately 16 kN. Importantly, the mechanical strength of these welds was benchmarked against relevant standards for the automotive and construction sectors, demonstrating that the spot welding with pinless tools enable achieving performance levels suitable for structural applications.

Keywords: friction stir spot welding; steel; high-strength steel; pinless tool; plate thickness

Academic Editor: Paul Kah

Received: 1 August 2025
Revised: 11 September 2025
Accepted: 14 September 2025
Published: 17 September 2025

Citation: Andrade, D.G.; Sabari, S.; Leitão, C.; Rodrigues, D.M. Assessment of Pinless Tools Efficiency in FSSW of Thick High-Strength Low-Alloy Steels for Structural Lap Joints. *J. Manuf. Mater. Process.* **2025**, *9*, 317. https://doi.org/10.3390/jmmp9090317

1. Introduction

Spot and lap welding remain among the most widely used joining methods in both the automotive and structural steel industries. In automotive manufacturing, each vehicle body typically contains thousands of spot welds due to their efficiency, speed, and cost-effectiveness, with resistance spot welding (RSW) being the most commonly adopted technology [1]. Beyond automotive applications, spot and plug welds are also extensively used in structural steel construction, particularly in cold-formed steel sections and diaphragm-braced systems, where they enable efficient load transfer and structural continuity [2–4]. According to Eurocode EN 1993-1-3 [5], arc spot welding is an approved method for joining thin-gauge steel elements, typically up to 4 mm in thickness. However, the growing use of lightweight materials in both sectors, such as aluminium and magnesium alloys, as well as advanced high-strength steels (AHSSs), demanded the research for new spot welding technologies, enabling the weldability constraints of those materials in fusion welding to be overcome. Some of the main weldability concerns in RSW of AHSSs are the formation of brittle structures in the fusion zone (FZ) of the welds, which may be accompanied by the presence of porosity and shrinkage voids, both promoting the interfacial

failure of the welds. This failure mode is considered a very detrimental characteristic of the spot welds for automotive applications, since it compromises the crashworthiness of the structure. Some AHSS grades may also display softening in the heat affected zone (HAZ), which despite enabling to avoid the failure of the resistance spot welds by interfacial failure, is detrimental in terms of the loading carrying capacity of the structure. Detailed information on the main weldability problems of AHSSs in RSW may be found in [6–10].

To prevent the above-described weldability constraints in RSW of AHSSs, in the last two decades, the solid-state friction stir spot welding (FSSW) process has been studied as an alternative to fusion spot welding. Feasibility studies were conducted to assess the suitability of FSSW technology for the joining of the M190 [11], DP 590 [12–14], DP600 [15], DP780 [16,17], DP 980 [18–20], DP1200 [21], TRIP [22–25], IF [14,26] and low-carbon [27–29] steels. In all these studies, the formation of an annular solid-state bond between the base materials was observed, as well as a fine-grained microstructure in the volume of material stirred by the tool. The annular bond geometry results from the plunging action of the tool pin, which in most of the works was reported to have a length superior to the upper plate thickness [11,12,15–17,21–25,29,30], generating a deep keyhole in the middle of the weld. To suppress the keyhole, special tools were developed, which enable to fill it with the material removed by the pin during the plunging stage. When using these special tools, the technology is renamed to refill FSSW (R-FSSW) [31–33]. However, this variant of the technology cannot be applied to high-strength and high-melting-point materials, such as steels. In conventional FSSW, the plunging and stirring action of the pin also promotes the upper flow of the lower plate base material, which may result in the formation of the well-known hook defect, with influence on the joints strength [12,22,34]. Although the hook and the annular bond geometry are both detrimental in terms of joint strength, the stirring action of the pin is very important for ensuring welding times in the range of 1 to 4 s [11,16,21,24,25]. These welding times are, in any case, much larger than those required for the joining by RSW, which are usually much shorter than 1 s for thin steel plates [1].

In addition to the deleterious effect of the pin on the joint morphology and strength, the wear of the pin during the joining of high-strength steels [19,20,35] is another important limitation to the industrial application of FSSW. Using PCBN tools, Feng et al. [11] reported the production of around 100 welds in M190 steel, without noticeable tool degradation, and Saunders et al. [18] reported the production of 900 welds in DP980 steel. Miles et al. [19] tested tools with varying contents of PCBN and W-Re to improve the tool toughness and were able to produce ~1200 welds in DP980 steel, using a tool with 70% PCBN. Choi et al. [35] were able to produce 500 spot welds in low-carbon steel using tungsten carbide (WC) tools. These authors analysed the evolution of tool geometry with pin wear and stated that the pin geometry should be established according to the worn geometry, for obtaining welds with consistent properties in large-scale production. However, despite the shortened electrode life also being concern in RSW of HSSs, due to the reaction of the zinc coating of the plates with the copper electrode, and due to the high welding forces required [36], a cost analysis revealed that for FSSW to be economically competitive with RSW, affordable and durable tool materials still need to be developed. According to Santella et al. [17], at the 2010 price, each FSSW tool should strive for around 26,000 spot welds to make the technology cost competitive with RSW.

One way of making the FSSW tools/process more affordable is to supress the pin, by producing cylindrical tools with a flat shoulder geometry. By suppressing the pin, not only is the most important factor in determining the tool wear/life suppressed, but the production cost of the tools is also decreased [37]. The use of pinless tools has already been investigated for the production of spot welds in aluminium alloys [38–45], steel [36,37,39,45–49] and dissimilar steel–aluminium [50,51] spot welds. Meanwhile, in the pinless FSSW (P-FSSW)

of aluminium alloys, several shoulder geometries were tested [52,53] in the welding of steels; due to its high strength, only flat shoulder geometries were used.

Many of the works in P-FSSW of steels report that the bonding between the plates is obtained by atomic diffusion, without any stirring of material through the plates interface [27,28,46,47]. Therefore, in most of the welds, the original interface between the plates is still visible in the macrographs after welding, due to the presence of local discontinuities and/or impurities, which are not disrupted and stirred during welding [46,48,49]. Obtaining suitable bonding, conducting to the plug failure of the welds in tensile shear loading, is still a challenge in P-FSSW research. This may be easily accomplished, but requires long welding times, up to 30 s [49,54]. In addition, some alternative welding procedures were developed, such as the pre-hole FSSW (PH-FSSW) [37] and the FSSW (PFFSW) projection [48] techniques. In PH-FSSW a trough hole is machined in the upper plate, at the spot welding location, before welding. The need for extra industrial operations, for producing the pre-hole, makes the PH-FSSW technique much expensive and time-consuming than the P-FSSW. In PFFSW, a special backing anvil is used, with a specially designed projection on the surface, which also increases the cost/complexity of the joining process.

While the use of pinless tools makes obtaining a continuous bonding between the plates very difficult, with very short welding times, it enables the suppression of the keyhole left by the pin, deeply increasing the dimension of the bonded interface relative to the spot welds obtained by conventional FSSW [47]. The use of pinless tools also enables the suppression of the formation of hook defects. By increasing the bonding area and suppressing the hooking defect, welds with strength much higher than those made by conventional FSSW may be obtained [37].

In this context, HC420LA steel was selected as the base material for this study. HC420LA is a high-strength low-alloy (HSLA) grade widely used in the automotive sector for safety-relevant components, owing to its favourable combination of strength, formability, and weldability. Beyond automotive use, HSLA steels such as HC420LA are also increasingly employed in lightweight structural applications, including cold-formed steel sections, where high load-bearing capacity with reduced thickness is required. This dual relevance makes HC420LA a representative and industrially important material for assessing the feasibility of P-FSSW in both automotive and structural contexts.

In the current work, multiple stacks of 1 mm thick HSLA420 steel sheets were joined using the P-FSSW technique to assess the maximum achievable weldable thickness under specific welding parameters. This represents a novel approach, as the existing literature on pinless tools primarily focuses on thin sheet applications. Here, applicability of P-FSSW was extended to multilayer configurations up to 4 mm total thickness, even under very short welding times (5–30 s), providing new insights into the limits of solid-state bonding without a pin. The study systematically explores the effects of stack thickness and welding time on joint quality, aiming to delineate the operational window of P-FSSW for high-strength steels. The main challenges encountered in achieving sound welds using pinless tools, such as the formation of interfacial discontinuities, insufficient bonding, and thermal management, were identified and critically analysed. This evaluation is particularly relevant for structural and automotive design, where the increasing demand for optimised, lightweight structures necessitates the spot welding of dissimilar materials and variable thickness combinations. These configurations remain a significant challenge for conventional resistance spot welding (RSW), which has not been fully resolved in the current literature [55–59]. Furthermore, to assess industrial viability, the mechanical performance of the welds was benchmarked against established design standards, namely AWS D8.1M [60] for automotive spot welding and EN 1993-1-3 [5] for structural applications in cold-formed steel. This combined technical

and regulatory benchmarking framework supports the broader adoption of P-FSSW in high-performance structural assemblies.

2. Experimental Procedure

The base material used in the investigation was the high-strength low-alloy steel HC420LA. Although this high-strength steel is widely employed in both automotive and structural applications, its performance under FSSW conditions remains insufficiently explored in the current literature. The mechanical properties and the chemical composition, as provided by the manufacturer of the HC420LA steel, are provided in Tables 1 and 2, respectively. Prior to welding, the surfaces of all steel sheets were polished using P4000 grit sandpaper to remove oxides and surface contaminants and then cleaned with ethanol to ensure a clean interface for diffusion bonding.

Table 1. Chemical composition of the HC420LA steel (wt%).

C	Mn	P	S	Si	Al	Nb	Ti
0.090	1.510	0.015	0.003	0.090	0.041	0.034	0.002

Table 2. Mechanical properties of the HC420LA steel.

Yield Stress [MPa]	Ultimate Tensile Strength [MPa]	Elongation [%]
437	566	22

Spot welding of HSLA420LA steel stacks, comprising two, three, or four sheets, each 1 mm thick, with dimensions 80 × 80 mm, was performed. The experimental setup and workflow are schematised in Figure 1. The plate stacks were clamped against a backing plate made of Inconel using two mechanical fasteners, positioned at a fixed distance of 20 mm from the tool centre. The spot welds were produced in position control, in an MTS I-STIR PDS machine, using a WC pinless tool, with a flat shoulder with 16 mm in diameter. To reduce manufacturing costs while maintaining tool performance, a modular design was adopted, where only the tool tip, which is in direct contact with the workpiece, was made of WC, while the tool holder was made from H13 tool steel. The WC tip and holder were machined with H9/d9 tolerance providing a free-running fit suitable for high-temperature variations. In addition, the WC tip tool was fixed in place using a lateral threaded pin, allowing secure attachment and easy replacement in cases of wear, as shown in Figure 2. A constant tool rotational speed of 1500 rpm was used. The tool diameter and the rotational speed were chosen, since in a previous investigation from the authors [61], it was found that a threshold in heat generation is reached when using these welding conditions in the spot joining of steels. By ensuring stable heat generation conditions, the influence of this factor on the heat and pressure distribution in the sheet stacks could be neglected in the current investigation.

The three-stage welding procedure adopted in conventional FSSW was also adopted, i.e., the welding operation consisted of the tool penetration, the dwell period, and the tool removal. A tool penetration of 0.5 mm and a plunging time of 4 s were set. Dwelling times of 1 s, 11 s, and 26 s were set, being tested for welding times of 5 s, 15 s, and 30 s, respectively. This procedure was established since, according to Lakshminarayanan et al. [27], the dwelling time is the most critical parameter in determining the lap joints shear strength. The evolution of the average temperature at the outer interface between the tool and the workpiece was recorded using a FLIR A655sc thermographic camera (FLIR, Wilsonville, OR, USA), positioned relative to the welding setup. Temperatures were acquired at a frequency of

25 Hz, and the emissivity was assumed to be 0.95, following the findings of a previous work by the authors [61].

Figure 1. Schematic representation of the experimental workflow used to assess the thermo-mechanical conditions during the P-FSSW process and to characterise the mechanical and microstructural properties of the resulting welds. (**a**) MTS I-STIR PDS FSW machine used to perform the spot welds; (**b**) schematic of the spot-welding process; (**c**) FLIR A655sc infrared thermographic camera for thermal cycle measurements during welding; (**d**) Shimadzu universal tensile testing machine for mechanical performance evaluation; (**e**) Shimadzu microhardness tester for hardness profiling; and (**f**) Leica optical microscope for microstructural characterisation.

Figure 2. Schematic representation of the pinless tool geometry, consisting of a tungsten carbide (WC) tip mounted in an H13 steel holder.

Following welding, the tensile shear test specimens were machined from the welded 80 × 80 mm plates with a final width of 30 mm, as illustrated in Figure 3a. The strength of the welds was evaluated by performing tensile shear tests, in quasi-static loading conditions (5 mm/min), using a Shimadzu AGS-X tensile testing machine (Shimadzu, Kyoto, Japan).

As shown in Figure 3, the number of stacked sheets was progressively increased to evaluate the evolution of joint strength and quality as a function of total stack thickness. Since welds between different numbers of sheets were studied, it was decided to always test the strength of the interface at the largest distance from the surface in contact with the tool, as schematised in Figure 3b–d. For each sample, to prevent bending during the tensile shear loading, sheet wedges with a thickness equal to that of the base material were glued to the ends of the samples to be loaded.

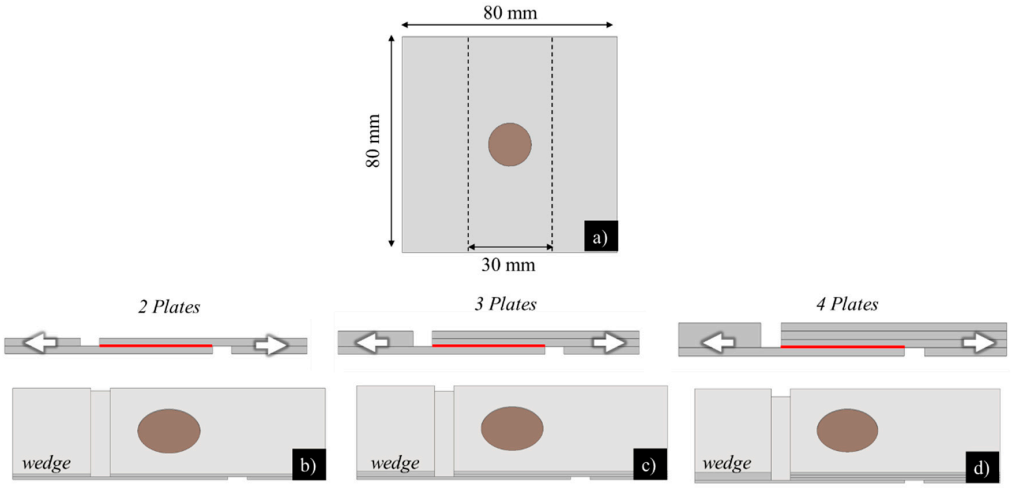

Figure 3. Schematic representation of the spot welds produced (**a**) and of the machined tensile shear test specimens used to evaluate their mechanical performance (**b**–**d**). Side views illustrate the lap joint configurations tested, consisting of two plates (**b**), three plates (**c**), and four plates (**d**), respectively. The red line indicates the interface subjected to tensile shear loading during testing.

To evaluate weld microstructure, transverse sections of the welds were prepared using standard metallographic procedures, etched with 2% Nital and observed using a Leica DM4000 M LED optical microscope (Leica, Wetzlar, Germany). Microhardness measurements were then performed using a Shimadzu microhardness tester, applying a load of 100 g with a dwell time of 15 s, to assess hardness gradients across the weld cross-sections.

The full matrix of welding parameters used in this study is summarised in Table 3. In the next, for identifying the welds, produced from stacks with a different number of sheets, the nomenclature Si_j will be used, where i represents the number of sheets in the stack and j represents the welding time. For example, S2_30 identifies a weld produced using a stack of two sheets and a welding time of 30 s.

Table 3. Summary of welding parameters.

Rotational Speed [rpm]	Plunge Depth [mm]	Plunge Time [s]	Total Welding [s]	Number of Sheets	Weld ID
1500	0.5	4	5	2	S2_5
				3	S3_5
				4	S4_5
			15	2	S2_15
				3	S3_15
				4	S4_15
			30	2	S2_30
				3	S3_30
				4	S4_30

3. Results and Discussion

This section presents a comprehensive analysis of the experimental results obtained from the spot welding of HSLA420 steel using pinless tools. The findings are structured into three main sections. First, the thermomechanical conditions developed during welding are examined through the analysis of torque and temperature evolution. Next, the morphological and microstructural characteristics of the welds are evaluated, with particular emphasis on the interface quality across different stack configurations. This is followed by an assessment of the mechanical performance of the joints based on tensile shear testing and microhardness profiles, providing insight into the influence of welding time and material thickness on joint strength and integrity. Finally, the industrial viability of the welds is evaluated through a comparative analysis against established automotive and structural design standards.

3.1. Analysis of the Thermo-Mechanical Conditions

Figures 4 and 5 show the evolution of the welding temperature and tool torque with time, for the welds produced using stacks of two, three, and four plates, for total welding times of 30, 15 s and 5 s. The temperature measurements were obtained via infrared thermography at the tool–workpiece interface, while torque data was directly extracted from the machine control system. Figure 4 shows that, in all cases, the thermal cycles follow a similar trend regardless of the number of plates used. During the initial plunging stage, a sharp rise in temperature is observed. For the 15 s and 30 s welds, the temperature rapidly stabilises at a steady state value of approximately 1200 °C once the dwell phase begins. In contrast, for the 5 s welds, no clear steady state is reached before the tool begins retracting, resulting in a sharp peak followed by a gradual cooling phase. Importantly, the number of stacked plates did not significantly affect either the peak temperature (in the 5 s welds) or the steady state temperature (in the 15 s and 30 s welds). Additionally, the cooling rates after tool retraction were nearly identical across all configurations. This suggests that, under the tested conditions, increasing the total plate thickness from 2 mm to 4 mm does not significantly alter heat dissipation at the surface. The only noticeable variation between the thermal cycles for different stack configurations occurred during the initial plunging phase. This deviation is not attributed to differences in stack thickness, but rather to machine vibrations during the onset of plunging and the modular construction of the tool system (Figure 2). The presence of small tolerances at the connection between the WC tip and the H13 tool holder may have introduced slight misalignments and mechanical instabilities, particularly at the beginning of the process, affecting heat generation.

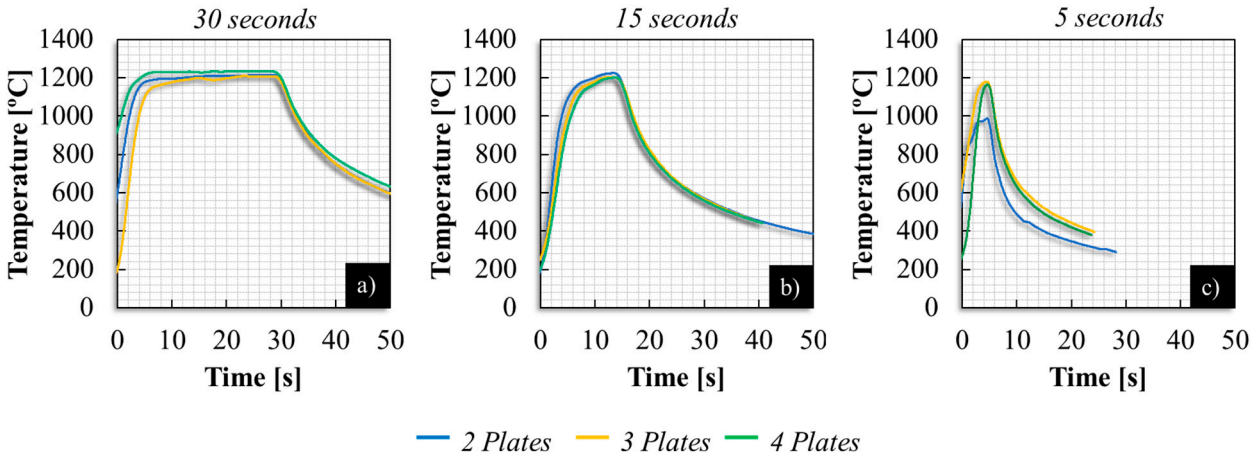

Figure 4. Temperature evolution during P-FSSW for stacks of two, three, and four plates at three welding times: (**a**) 30 s, (**b**) 15 s, and (**c**) 5 s.

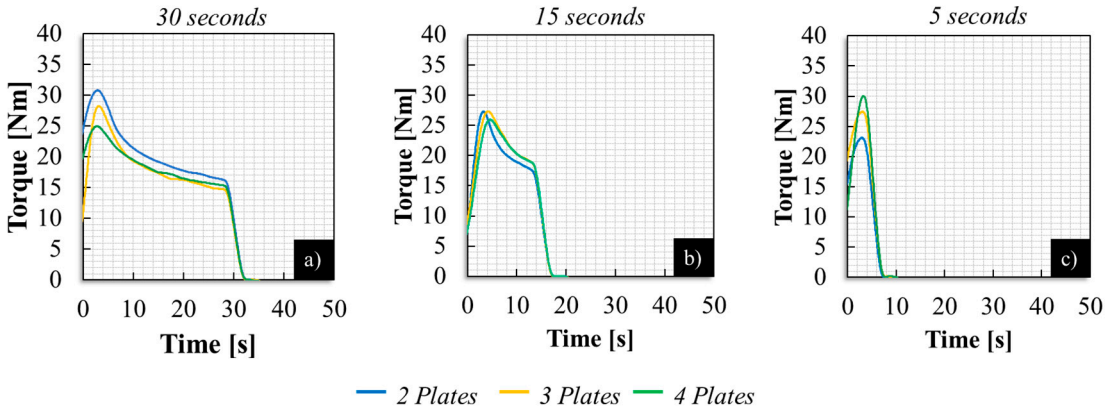

Figure 5. Torque evolution during P-FSSW for stacks of two, three, and four plates at three welding times: (**a**) 30 s, (**b**) 15 s, and (**c**) 5 s.

Similarly, the analysis of tool torque evolution over time reveals consistent behaviour across all tested conditions, indicating that the number of stacked plates had a negligible influence on the torque response during welding. In all cases, the torque rapidly increases during the initial plunging stage, reaching a maximum value near the end of the penetration phase. For the longer welding times (15 s and 30 s), as the material beneath the tool becomes thermally softened, the torque gradually decreases and stabilises at a steady state value during the dwell phase. This behaviour is consistent with the temperature trends shown in Figure 4, where thermal equilibrium is achieved after the plunging stage. The torque reduction is indicative of reduced flow stress in the material as welding progresses. As registered for the thermal cycles, the only noticeable variation between joint configurations occurs during the initial plunging phase, for which small differences in peak torque may be observed. Once again, these are attributed to the vibrations in the FSW machine and the mechanical tolerances associated with the modular tool design. These observations indicate that, under the tested conditions, variations in the number of stacked plates had a limited effect on the thermal and mechanical responses measured at the tool–workpiece interface. This consistency enables a more isolated assessment of how welding time and stack configuration influence the resulting weld morphology and microstructure in the subsequent analysis.

3.2. Morphological and Microstructural Analysis

Figure 6 shows the cross-sectional macrographs of all welds produced in this study, illustrating the influence of dwell time and stack thickness on weld morphology. For all welds, a distinct process affected zone (PAZ) can be observed, exhibiting a semi elliptical morphology and a microstructural contrast relative to the surrounding base material. Notably, none of the welds display a stirred nugget region typical of conventional FSSW. Instead, straight dark lines are visible along the original interface between the stacked sheets. The linearity and continuity of this interface indicate the absence of through thickness stirring, confirming that material transport across the joint was negligible and that bonding is governed primarily by diffusion-based mechanisms. Also, the PAZ morphology was approximately symmetric about the tool axis, which indicates that the process conditions were stable and that heat input and material deformation were uniformly distributed around the weld centre. Owing to the absence of the tool pin, the weld cross-sections exhibit no noticeable reduction in thickness, internal cavities, or hooking defects typically associated with pin induced material flow. In all cases, the PAZ extended through the full cross-section of the plates; however, in the four-plate welds, the PAZ, and consequently the width of the bonded interface, was significantly reduced in the deepest interfaces.

Moreover, increasing dwell time resulted in a larger PAZ, reflecting the higher heat input. The only geometric alteration observed is a shallow surface indentation caused by the 0.5 mm tool penetration during the plunging phase. Among all tested conditions, the S2_5 sample, produced with the shortest welding time and thinnest plate stack, exhibits the most pronounced morphological deviation. Specifically, an upward displacement of the top plate material is visible near the shoulder edge, locally decreasing the sheet thickness.

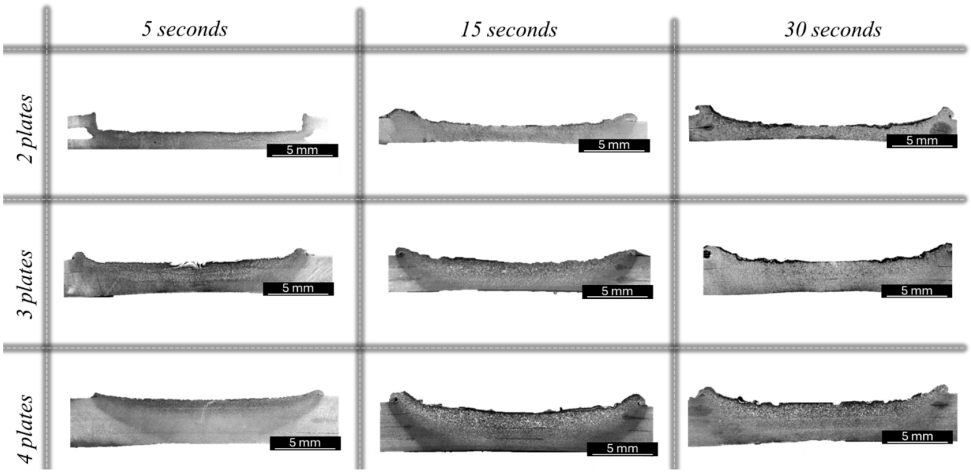

Figure 6. Cross-sectional macrographs of P-FSSW joints produced with different stacking configurations and welding times: (left to right) 5 s, 15 s, and 30 s; (top to bottom) two, three, and four stacked plates.

Figure 7 presents a detailed microstructural analysis of the S4_5 weld condition, which represents the most critical combination of parameters investigated in this work, namely the shortest welding time and the highest stack thickness. Figure 7a displays the full cross-section of the weld, while Figure 7b–d show the microstructural evolution at the mid plane of the weld, focusing on the interfaces between successive plate layers: specifically, the first and second plates (Figure 7b), second and third plates (Figure 7c), and third and fourth plates (Figure 7d). Higher magnification micrographs of these regions are shown in Figure 7e–g, respectively, highlighting the weld interface zones extracted from the dashed regions marked in the low-magnification images.

The microstructural observations reveal that the limited welding time exerts a substantial influence on the thermal gradient across the weld thickness, resulting in significant variation in grain morphology from the top to the bottom of the joint. At the upper interface, directly contacted by the rotating tool shoulder, the microstructure consists of a non-equiaxed mixture of acicular ferrite and dispersed fine bainitic grains within a ferritic matrix. This structure is consistent with high peak temperatures and rapid cooling, characteristic of friction-based welding processes.

According to Chen et al. [62], the ratio between bainitic and ferritic phases in recrystallised structures is predominantly affected by the austenite grain size, the cooling rate, and the extent of niobium precipitation. The austenite grain size is determined mainly by the austenitisation temperature, with coarser grains favouring bainite formation. Rapid cooling, in turn, supports bainitic transformation. Niobium precipitates, often in the form of carbides (NbC) or carbonitrides (NbCN), inhibit recrystallisation when segregated at grain boundaries, simultaneously preventing grain growth and providing nucleation sites for acicular ferrite formation [63,64]. However, at high peak temperatures exceeding ~1150 °C, recrystallisation is accelerated and can outpace niobium precipitation. At even higher temperatures (>1200 °C), complete redissolution of Nb(C,N) precipitates can occur, as noted by Wang et al. [65]. The observed microstructure in the upper region of the S4_5

weld suggests that, due to the short welding time and larger thermal mass of the four-sheet stack, a sufficient temperature to partially dissolve niobium precipitates may have been reached only near the upper interface, leading to the observed heterogeneous mixture of bainite and ferrite.

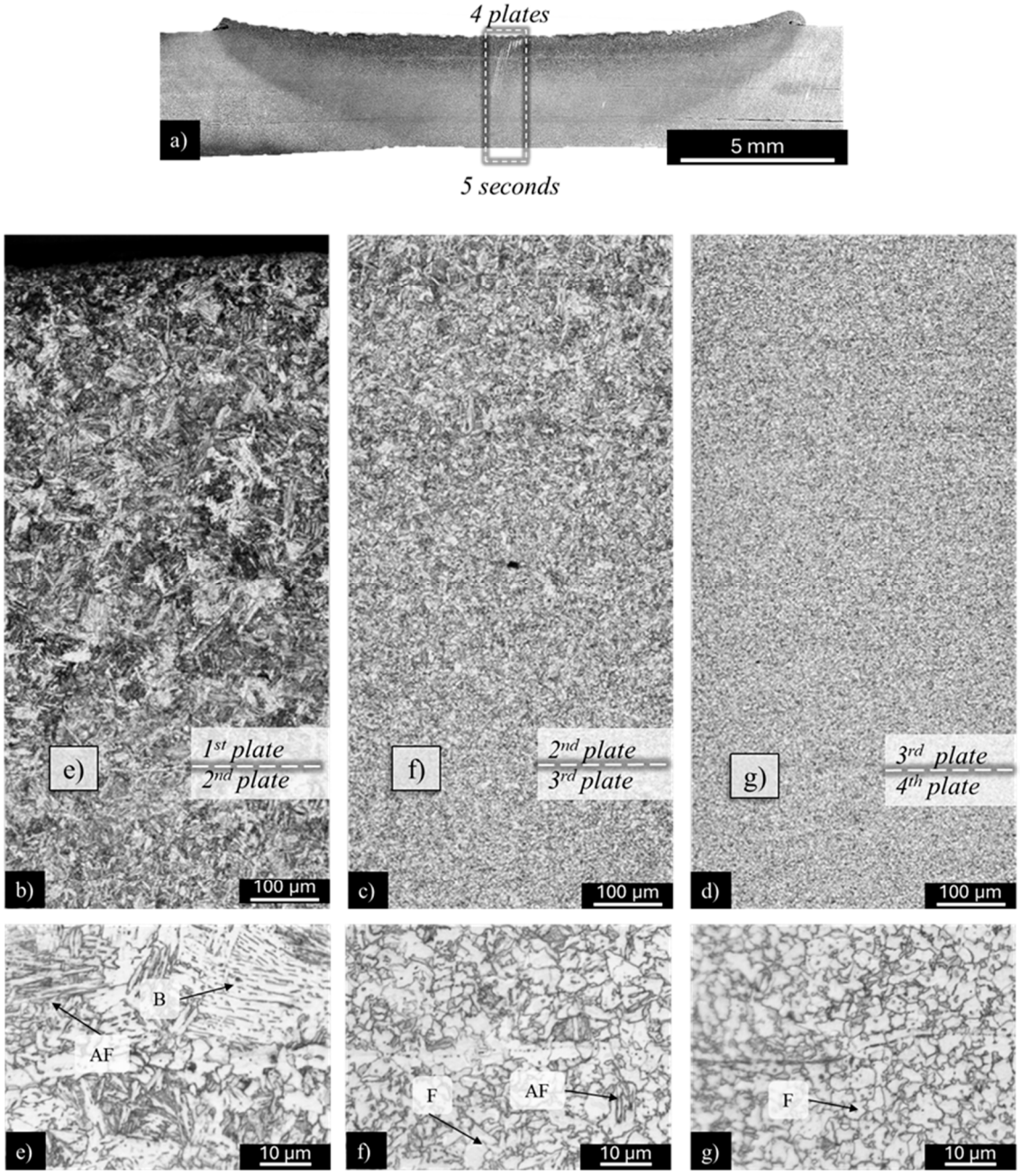

Figure 7. Microstructural characterisation of the S4_5 weld, produced using four stacked plates and 5 s of welding time: (**a**) macrograph of the weld cross-section showing the region analysed; (**b**–**d**) optical micrographs of the interfaces between the first and second plates (**b**), second and third plates (**c**), and third and fourth plates (**d**); (**e**–**g**) high-magnification micrographs of the respective interfaces. Labels B, AF, and F indicate bainite, acicular ferrite, and ferrite, respectively.

In the second plate layer, a notable grain refinement is observed relative to the upper plate, indicating the effect of a thermal gradient along the weld thickness. This is consistent with reduced exposure to peak temperatures and limited dwell time. According to Zurob et al. [66], at temperatures below ~1150 °C, precipitation and recrystallisation occur concurrently. In such conditions, grain growth is controlled by a competition between the

driving force for recrystallisation and the pinning effect of Nb(C,N) precipitates. When recrystallisation overcomes this inhibition, moderate grain growth can occur, leading to the fine-grained structures observed in this region.

Finally, the microstructure in the third (bottom) plate of the S4_5 weld, is predominantly ferritic, with a combination of acicular and polygonal ferrite. The low fraction of acicular features and limited grain refinement suggest that this region experienced thermal cycles close to, but not significantly above, the critical recrystallisation temperature. The resulting grain size is comparable to that of the base metal, indicating that the heat input in this region was marginally sufficient for partial recrystallisation but insufficient for extensive phase transformation.

Additionally, the high magnification micrographs taken at the interfaces between the stacked plates (Figure 7e–g) confirm the presence of continuous metallurgical bonding and microstructural continuity across all joints, even for the interface farthest from the tool–workpiece contact surface. Despite the short welding time of 5 s used in the S4_5 condition, successful bonding was achieved across all interfaces. However, it is noteworthy that, at the interface between the third and fourth plates (Figure 7g), some microstructural discontinuities and trapped inclusions may be observed. These may be attributed to the reduced temperature and pressure levels at the bottom of the stack, which can limit the extent of plastic deformation and interfacial diffusion. Additionally, the short exposure time to elevated temperatures may not have been sufficient to fully disrupt surface oxides or eliminate initial gaps between the plates, thus reducing bonding effectiveness in this region.

To further evaluate the bonding quality at the most distant interface from the tool, Figure 8 presents high-magnification micrographs of the obtained bonds for all weld conditions. This region was selected due to its limited exposure to direct heat and pressure input, making it the most critical zone for assessing joint integrity, particularly in configurations with three and four stacked plates. Across all conditions, the presence of well-defined ferrite grains at the interface indicates that metallurgical bonding was achieved through solid-state welding, even in the absence of significant plastic deformation. This observation is consistent with the lack of mechanical stirring due to the pinless tool design. Adjacent to the interface, regions often display disorganised and multidirectional ferritic structures typical of acicular ferrite, highlighting the localised thermal cycles and microstructural heterogeneity along the weld thickness.

Notably, welds produced with longer dwell times of 30 s tend to exhibit coarser grain structures, consistent with higher thermal exposure and extended diffusion times at the interfaces. In contrast, welds generated with shorter welding times (5 s) and higher stack configurations (three and four plates) show more refined microstructures, indicative of reduced thermal input and shorter diffusion durations between plates. This trend is particularly evident at the lower interfaces of the S3_5 and S4_5 welds, where localised discontinuities are observed, potentially associated with insufficient thermal activation for effective bonding.

Additionally, in the S3_30 weld, a distinct dark interfacial layer was observed. Figure 9 presents the SEM/EDS analysis of this dark region, which reveals continuous grains extending across the interface, providing clear evidence of metallurgical bonding. The corresponding EDS spectrum indicates that the detected elements are primarily those of the base steel (Fe, Mn, C), together with alloying elements consistent with the nominal chemical composition of HC420LA steel (Table 1). However, the presence of elevated carbon and oxygen signals suggests that the dark phases correspond to oxide inclusions rather than voids or lack of bonding. These inclusions are most likely associated with insufficient surface preparation, compounded by the absence of mechanical stirring inherent to the

pinless tool configuration. Such features may locally impair joint performance and highlight the critical importance of rigorous surface cleaning in welding processes where interfacial mixing is not promoted by the tool geometry.

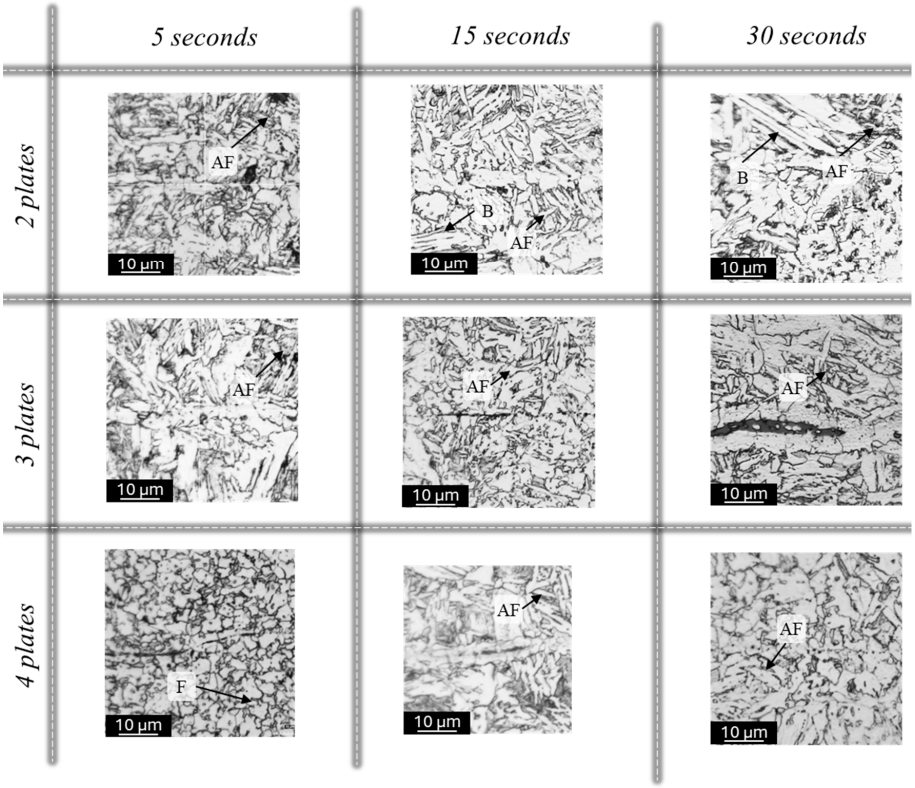

Figure 8. High magnification micrographs of the lowermost interfacial regions between plates for all weld conditions: welds produced with two plates (S2_5, S2_15, S2_30), welds with three plates (S3_5, S3_15, S3_30), and welds with four plates (S4_5, S4_15, S4_30). Labels B, AF, and F indicate bainite, acicular ferrite, and ferrite, respectively.

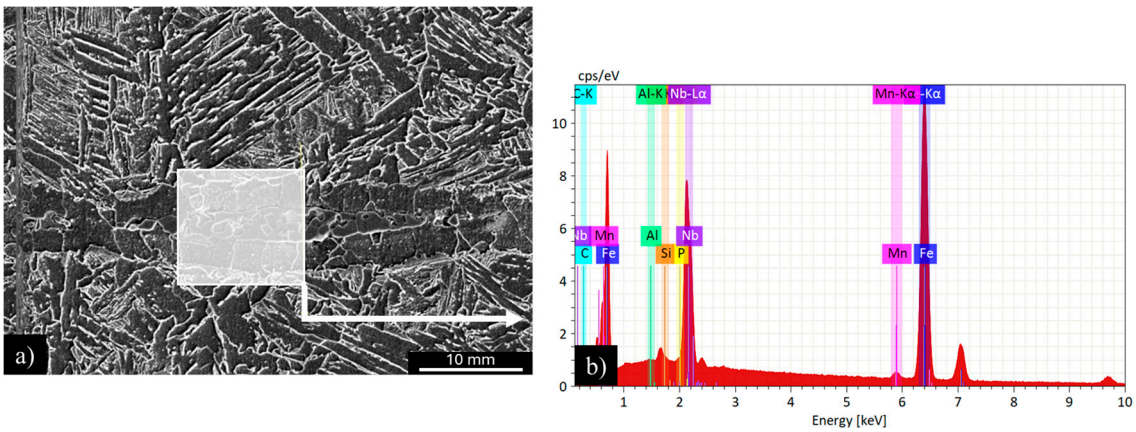

Figure 9. SEM/EDS characterisation of the weld interface in sample S3_30: (**a**) SEM cross-sectional micrograph s; (**b**) EDS spectrum acquired from the interface dark region.

3.3. Mechanical Characterisation

Figure 10 presents the hardness profiles along the vertical direction of the welds, measured at mid width (as illustrated in Figure 10a). The arrow in Figure 10a indicates the measurement path, from the top surface of the weld to the bottom plate. Profiles are shown for samples welded with two, three, and four stacked plates and varying dwell times (5,

15, and 30 s). The reference hardness of the base material (BM) is also indicated in each graph for comparison. According to the figure, a consistent trend is observed across all conditions, i.e., the hardness progressively decreases from the top to the bottom of the weld (Figure 10b–d). This gradient is attributed to the microstructural variation observed along the weld thickness, where regions closer to the tool shoulder exhibited a non-equiaxed microstructure composed of acicular ferrite and dispersed fine bainitic grains. In contrast, the lower hardness values in the bottom plates correspond to a predominantly ferritic microstructure. All welds exhibit hardness values above the BM reference throughout the weld thickness, demonstrating that the entire stack was thermally and mechanically affected by the welding process, regardless of the number of plates used. The lowest hardness value, approximately 180 $HV_{0.1}$, was recorded at the bottom of the S4_5 weld, while the highest value, around 325 $HV_{0.1}$, was measured near the surface of the same weld. This substantial variation reflects the steep thermal gradient induced during the short welding cycle in the thickest configuration.

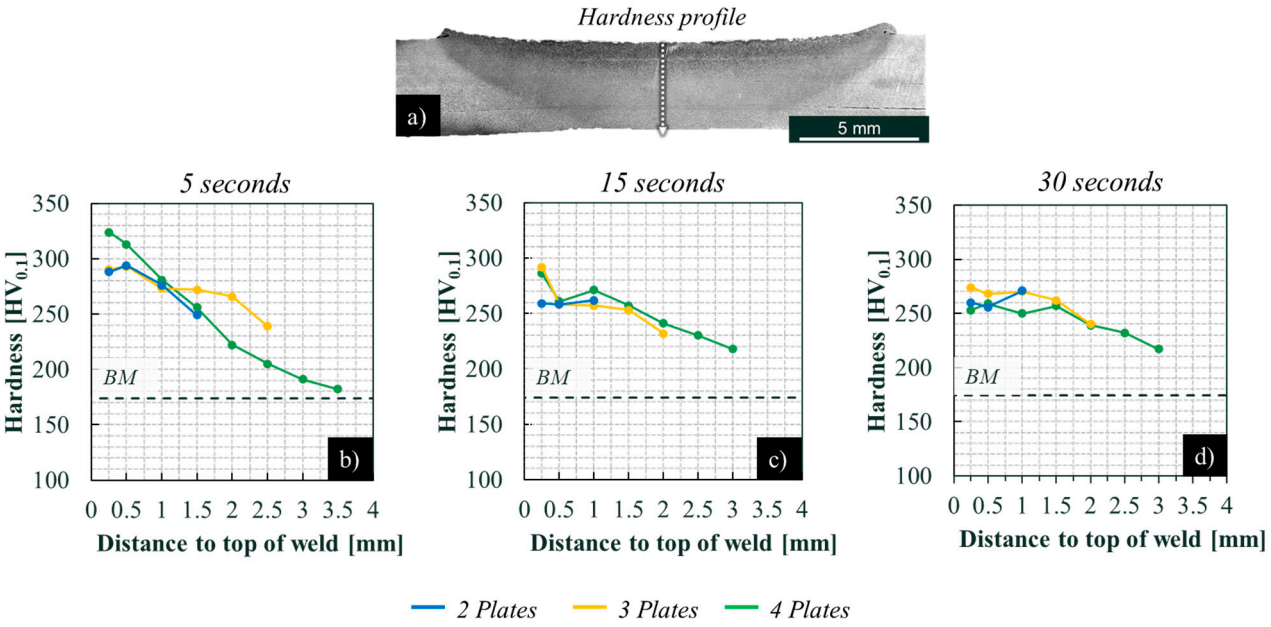

Figure 10. Microhardness profiles along the vertical direction, as indicated in (**a**), for welds produced with dwell times of (**b**) 5 s, (**c**) 15 s, and (**d**) 30 s, using different plate stacking configurations (two, three, and four plates).

Moreover, the hardness profiles for the 15 s and 30 s welds show remarkably similar trends and magnitudes across all stack configurations. This indicates that, beyond a certain dwell time threshold, further increases in welding time do not significantly affect the final hardness profile. This result is particularly relevant for industrial applications where reducing cycle time is critical for productivity. Additionally, the nearly overlapping hardness curves across different stack thicknesses, for the same dwell time, further support the conclusion that the number of plates had a negligible effect on heat dissipation and hardness evolution under the tested conditions.

The tensile shear test results presented in Figures 11 and 12 provide critical insight into the mechanical performance of the joints under varying welding times and stack configurations. Figure 11 shows the force–displacement curves for all welds, along with benchmark results for the base material tested in two different specimen widths of 30 mm (matching the specimen geometry used for weld testing as shown in Figure 3) and 16 mm (equivalent to the tool shoulder diameter). These baseline curves offer a reference for interpreting the mechanical integrity of the welds relative to the HSLA420 base material.

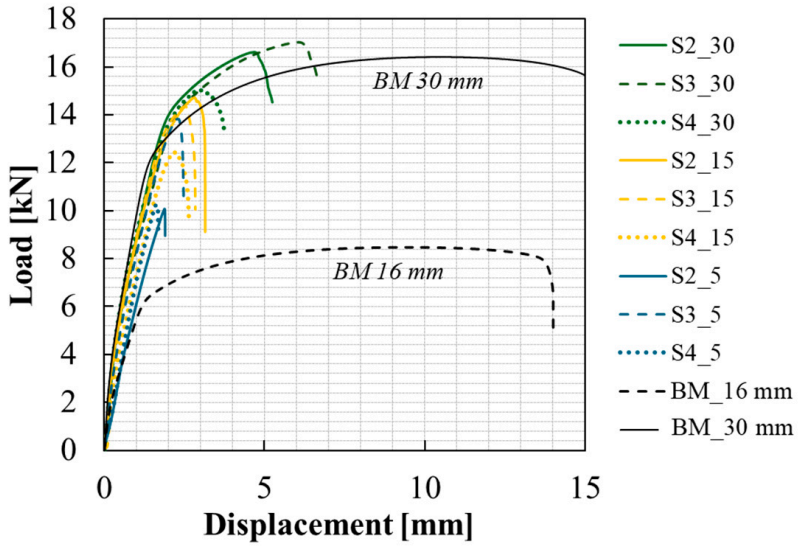

Figure 11. Force–displacement curves obtained from tensile shear tests for all weld conditions, compared against tests performed on the base material using specimens with widths of 16 mm and 30 mm.

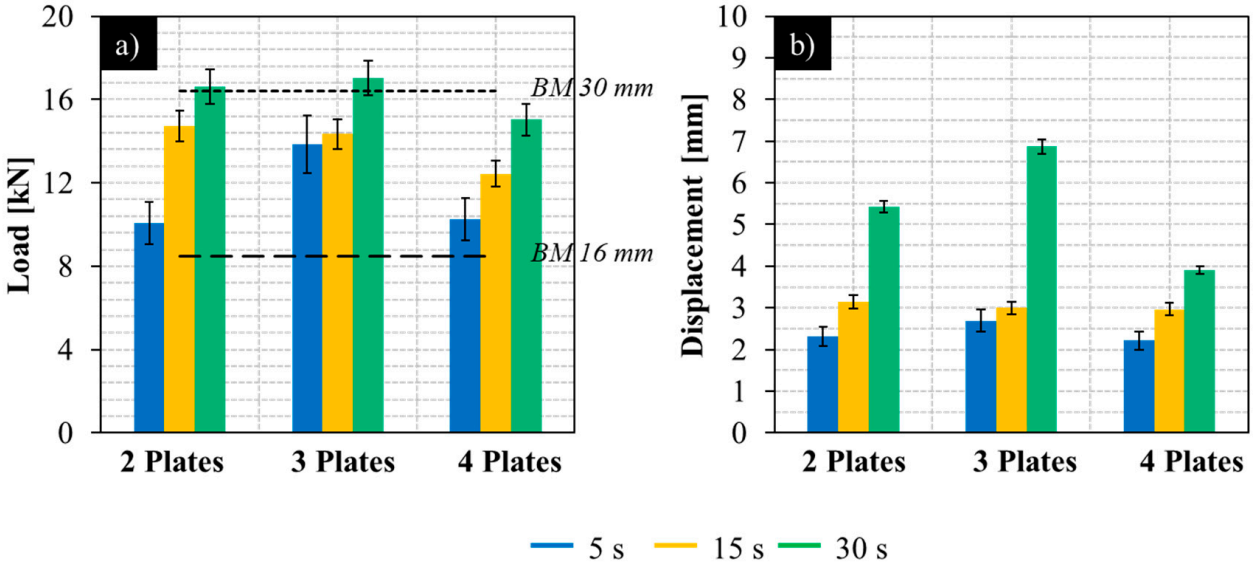

Figure 12. Summary of mechanical performance results extracted from tensile shear tests for all weld conditions: (**a**) maximum tensile force and (**b**) maximum displacement at failure, as a function of the number of stacked plates and welding time (5, 15, and 30 s). The dashed lines represent the maximum force recorded for the base material samples with 30 and 16 mm widths.

All the curves in Figure 11 begin with a linear force–displacement relationship, indicative of elastic deformation. Notably, all welds produced with a 5 s dwell time, as well as the S4_15 weld, failed within this linear regime, suggesting that these joints did not reach plastic deformation before failure. This premature failure highlights the limited bonding strength achieved under short processing times, particularly in configurations with four plates. Despite this, even the weakest welds (e.g., S4_5 and S3_5) exhibited higher ultimate loads than the base material tested with a 16 mm width, implying that a certain degree of bonding occurred at the joint interface. The elevated load-bearing capacity observed in these welds may also be partially attributed to the increased hardness levels recorded across the PAZ, in relation to the base material. In contrast, the welds produced with 15 s and especially 30 s dwell times, independently of the number of stacked plates, showed

ductile behaviour, with force–displacement curves extending well into the plastic regime prior to failure. These results confirm that the longer welding times provided adequate thermal and mechanical energy to activate solid-state welding and generate structurally sound joints.

Figure 12 summarises the maximum force and corresponding displacement for each weld configuration. The data reinforce the conclusion that the welding time is the dominant factor controlling joint strength. A clear trend is observed, where increasing the dwell time enhances both strength and ductility of the welds. Welds fabricated with a 30 s dwell time consistently achieved the highest peak forces and largest displacements, regardless of the number of stacked plates. On the other hand, increasing the number of stacked plates had a secondary, yet measurable impact. Generally, the welds involving four plates (S4_x) showed the lowest mechanical performance among the samples within each dwell time category. This trend can be associated with the lower thermal exposure at the farthest interfaces from the tool, particularly under short welding durations, as well as the presence of the microstructural discontinuities observed in the metallographic analyses (Figure 8). Figure 12b shows that the highest ductility was obtained for the S2_30 and S3_30 welds, which also exhibited the highest strength. Conversely, the lowest ductility was registered for the S4_5 and S4_15 welds.

Despite the important differences in strength and ductility, all the welds tested exhibited interfacial fracture during the tensile shear tests. This is exemplified in Figure 13a, which shows the top and bottom plates of a representative sample after testing. In the top plate image, the original bonded interface area is highlighted by a red dashed contour, while the bonded region just before the sample failure is marked in blue. This shows that the bond between the two plates was not uniform across the joint interface. According to the image, sample failure started at the weld periphery, where the bonding appears to be weaker, and propagated inward. The central region of the weld, which sustained the final load, showed significant plastic deformation for all tested samples. This post-fracture weld morphology shows that the absence of the stirring action of the pin, in pinless welding, promotes non-uniform bonding across the joint. The same conclusion was reached when analysing the bond interface in the metallographic analysis. However, even in the absence of non-uniform bonding, the welds may fail after plastic deformation, as shown in Figure 11.

The initial diameter of the bonded interface was measured for each welding condition, using the samples tested until failure, and the results are plotted in Figure 13b. These measurements indicate that, for all stack configurations, the interface diameter increases with the welding time, reflecting more extensive thermal and pressure exposure. For the 15 s and 30 s welding times, the bonded diameter decreases with increasing stack thickness, due to the bowl shape heat distribution, which can be depicted from the shape of the process affected zone depictable in the cross-sections of the welds in Figure 6. An exception to this trend was registered for the 5 s condition, in which the three-plate stack yielded a larger interface diameter than the two- and four-plate stacks. These results suggest that the very short maintenance time of 1 s, for the 5 s welding condition, does not enable uniform heat and pressure distribution to be attained, giving rise to welds with less uniform properties. However, since lower bonded areas were observed for both the two- and four-plate stacks, the results indicate that plate thickness is not the main cause of process instability. Some reasons for process instability were provided in Section 3.1, when analysing the torque evolution with time, for the different welding conditions.

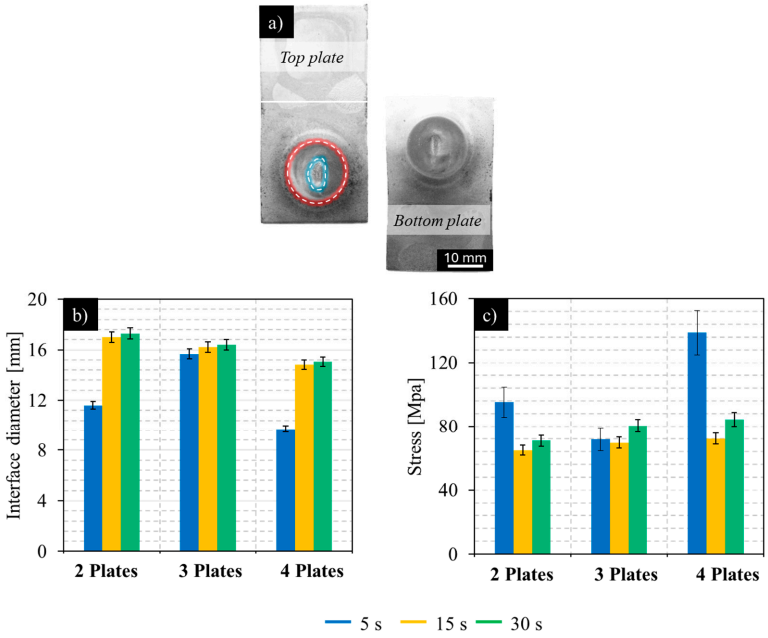

Figure 13. (**a**) Example of fracture surfaces after tensile shear testing, (**b**) measured interface diameter, and (**c**) average shear stress at the interface as a function of welding time and stack configuration.

Based on the measured interface diameters (Figure 13b), the average shear stress at failure was calculated for each weld by dividing the peak force (Figure 12a) recorded during testing by the corresponding initial bonded area (as highlighted by the red circle in Figure 13a). The results are presented in Figure 13c. For the 15 s and 30 s welding times, the average shear stress values were relatively consistent across all stack configurations, indicating comparable interfacial strength among the different welding conditions, i.e., comparable bond strength with increasing plate thickness. The lower interface area, registered for the two- and four-plate stacks, for the 5 s welding condition, is the reason why the calculated interface shear strength is comparatively higher for these welds. Despite the mismatch in properties observed for the S2_5 and S4_5 welding conditions, the consistent results obtained for the other configurations indicate that pinless tools can be applied to welding plates thicker than 3 mm. Using a bulk tool and ensuring the plates flatness, for avoiding instabilities at the beginning of the welding process, as well as ensuring good quality surfaces, perfectly clean of oxides and other contaminants, will strongly contribute to enhance the quality of the joints relative to the ones produced in the current work.

3.4. Validation of Weld Performance Against Automotive and Structural Standards

To assess the effectiveness of using spot welding with pinless tools in automotive and structural applications, the mechanical performance of the welds was benchmarked against the minimum requirements set by relevant standards. Specifically, the AWS D8.1M [60] and EN 1993-1-3 [5] standards for automotive and structural applications, respectively, were considered. These standards provide the minimum allowable shear strength for the reliable use of spot welds in thin-gauge high-strength steels. By comparing the maximum shear loads, determined in the current work for the tested spot welds, to the prescribed thresholds, the compliance and potential of the produced lap joints were evaluated.

The AWS D8.1M [60] standard provides an empirical expression to estimate the minimum acceptable static shear strength ST (in kN) of a spot weld, based on the base metal tensile strength S (in MPa) and on the minimum sheet thickness t (in mm), as follows:

$$ST = \frac{\left(-8.83 \times 10^{-7} \times S^2 + 1.34 \times 10^{-3} \times S + 1.514\right) \times S \times 4t^{1.5}}{1000}. \quad (1)$$

According to the previous equation, with the mechanical properties of the base metal provided in Table 2 (S = 566 MPa) and considering the minimum plate thickness (t = 1 mm), the minimum acceptable shear strength for a spot weld is calculated to be approximately 4.5 kN. When comparing this threshold to the experimental results presented in Figure 12, it is evident that all welds produced exceed the standard minimum strength requirement.

The results obtained in this study were further extended to a broader set of lap joint configurations, as shown in Figure 14a, which presents the evolution, with the plate thickness, of the minimum required shear strength calculated using Equation (1) for the HC420LA steel (red dashed curve). The diagram delineates two performance regions, i.e., a compliant zone (highlighted in green), where the experimentally measured shear loads exceed the minimum strength requirement, and a "non-compliant zone" (highlighted in red), where the welds fail to meet the specified threshold. Superimposed on this curve are the shear strength values measured for different stack configurations and welding times (5, 15, and 30 s). The weld strength was plotted against the maximum section thickness of the lap joints, i.e., 1 mm for S2_X joints, 2 mm for S3_X joints, and 3 mm for S4_X joints. This extrapolation relies on the assumption that the thermal and pressure conditions in pinless welding are independent of the thickness, in the studied range, since similar bond strength was obtained for the S2 and S4 welds. By using the experimental results from known configurations, as representative of thicker assemblies, the study establishes a conservative performance envelope for a broader range of structural joint scenarios.

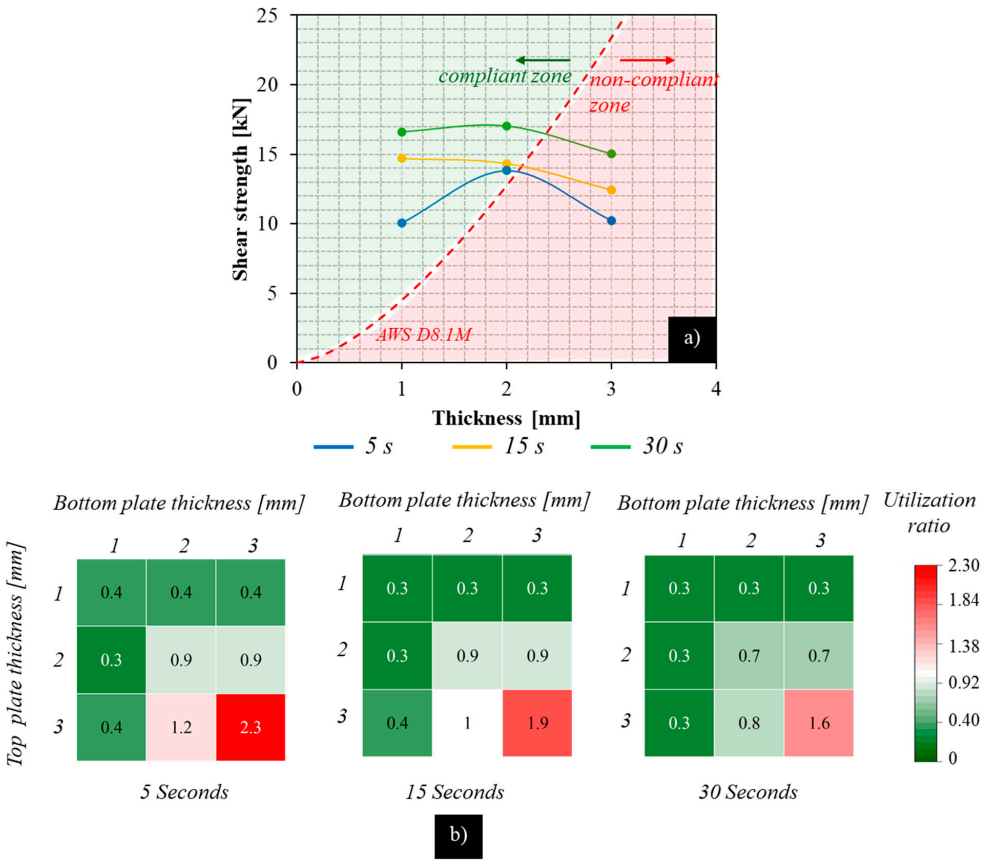

Figure 14. (**a**) Comparison between the experimentally measured shear strengths of the lap joints and the minimum strength requirements defined by the AWS D8.1M [60] standard. (**b**) Utilisation ratio matrix for various plate stacking configurations, showing compliance (green) and non-compliance (red) for 5 s, 15 s, and 30 s welds.

Using the same assumptions described above, Figure 14b presents a utilisation ratio analysis, in which the ratio is defined as the minimum required shear strength, calculated

according to AWS D8.1M [60], divided by the experimentally measured shear strength for each spot weld (Figure 12). This comparison was extended to include hypothetical lap joint configurations with top and bottom plate thicknesses ranging from 1 to 3 mm. The results are represented in a utilisation ratio matrix, where green cells indicate compliant joints (utilisation ratio < 1), and red cells highlight configurations that fail to meet the minimum shear strength requirements (utilisation ratio > 1).

This analysis suggests that the spot welds can reliably meet AWS strength criteria for a wide range of stack configurations, particularly when sufficient welding time is applied. Specifically, for welding conditions of 15 s and 30 s, all evaluated thickness combinations, except the most extreme case (3 mm top and 3 mm bottom plates), result in compliant joints. In contrast, for the shortest welding time of 5 s, the process also fails to meet the strength requirements for the configuration with a 3 mm top plate and a 2 mm bottom plate.

To extend the benchmarking of the spot welds performance to structural applications, the lap joint strength was also compared with the minimum shear resistance requirements outlined in EN 1993-1-3 [5]. According to the standard, the shear resistance $F_{v,Rd}$ (in kN) of a spot weld is given by

$$F_{v,Rd} = \frac{\pi}{4} d_s^2 f_u / \gamma_{M2}, \quad (2)$$

in which, for spot welds produced by RSW, the effective weld diameter is given by $d_s = 5\sqrt{t}$ (in mm), based on the minimum plate thickness t and f_u (in MPa) is the ultimate tensile strength of the base material and $\gamma_{M2} = 1.25$ is the partial safety factor.

According to Equation (2) and based on the mechanical properties of the base metal reported in Table 2, as well as on the minimum plate thickness of 1 mm, the minimum allowable shear resistance per EN 1993-1-3 is estimated at approximately 8.89 kN. When this threshold is compared to the experimentally measured shear strengths shown in Figure 12, it is evident that all weld configurations exceed the minimum requirement set for RSW joints.

Similarly to the analysis conducted to plot Figure 14, Figure 15a presents a comparison between the experimentally measured shear strengths of the lap joints tested in the current work and the minimum required shear resistance calculated using the EN 1993-1-3 formulation for resistance spot welds. The results are shown for different plate stacking configurations and welding times. The dashed red line delineates the threshold set by the standard, representing the compliance boundary. To complement this, Figure 15b provides the utilisation ratio matrix, calculated as the ratio of the Eurocode-required shear resistance to the experimental strength. Green coloured cells (utilisation ratio < 1.0) denote compliant joints, while red tones (utilisation ratio > 1.0) signal configurations that do not meet the minimum requirements.

The results reveal that joints produced with dwell times of 30 s generally achieve compliance across most tested configurations, except for those involving a 3 mm top plate combined with 2 mm or 3 mm bottom plates. Conversely, welds produced with shorter dwell times of 15 s and 5 s only met the design standard when the minimum plate thickness in the configuration was 1 mm, regardless of its position in the stack. This highlights the limitations of short welding durations in achieving structurally compliant joints, suggesting that increased thermal input or optimised tool strategies may be necessary to meet design requirements in thicker configurations. Alternatively, improving the joint performance under faster welding cycles may be achieved by increasing the number of welds per joint, thereby distributing the load more effectively across the connection.

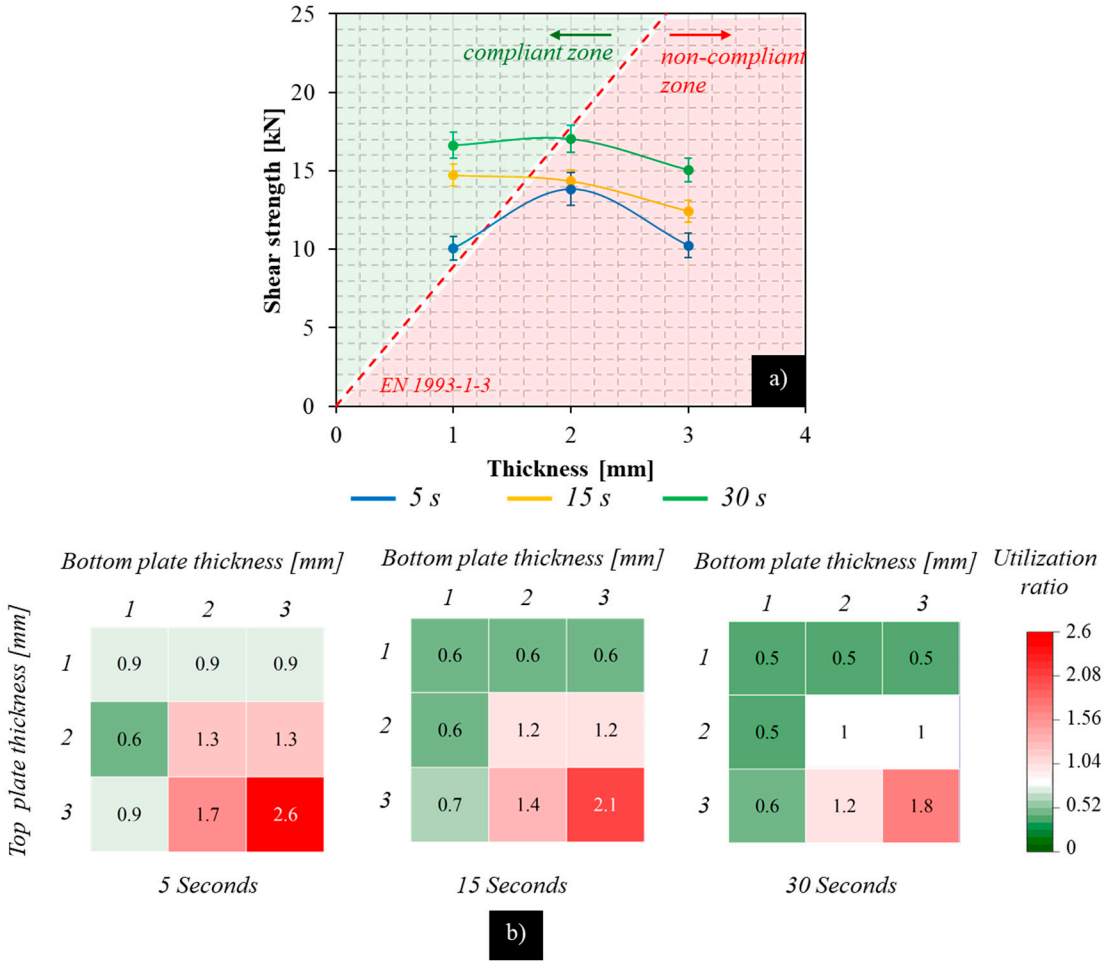

Figure 15. (**a**) Comparison between the experimentally measured shear strengths of the P-FSSW lap joints and the minimum strength requirements defined by the EN 1993-1-3 [5] standard. (**b**) Utilisation ratio matrix for various plate stacking configurations, showing compliance (green) and non-compliance (red) for 5 s, 15 s, and 30 s welds.

4. Conclusions

This study evaluated the feasibility and performance of P-FSSW applied to multi-stack configurations of HC420LA steel sheets. The influence of welding time (5, 15, and 30 s) and stack thickness (two, three, and four plates) was systematically assessed. The following conclusions can be drawn:

- Thermal cycles and torque profiles revealed consistent behaviour across all configurations, with only minor variations observed during the plunging phase. The number of stacked plates had a negligible effect on heat and torque evolution under the selected process parameters, indicating stable process control.
- Macrostructural observations confirmed the absence of material stirring across the plates interface. Instead, metallurgical bonding was achieved along the original plate interfaces via solid state bonding, resulting in a distinct semi elliptical process affected zone. Despite the absence of plastic flow or stirring, bonding was achieved, though localised impurities and discontinuities were more prevalent at deeper interfaces, especially in four plate welds with 5 s dwell time.
- Weld hardness exceeded that of the base material (180 HV0.1) across all conditions, reflecting the combined thermal and mechanical influence of P-FSSW. Maximum hardness values reached ~325 HV0.1 near the weld surface in the S4_5 condition.

- Tensile shear results demonstrated a strong dependence on dwell time. Welds produced at 5 s exhibited limited strength and ductility, while those at 15 and especially 30 s showed significantly higher loads and displacements, with the S3_30 configuration reaching a maximum strength of 16.5 kN and displacements above 5 mm. The number of stacked plates only had a secondary influence on the mechanical properties.
- The mechanical performance of the P-FSSW joints was benchmarked against AWS D8.1M and EN 1993-1-3 standards, demonstrating that most of the welds produced with 30 s dwell times comply with the minimum shear strength requirements of both standards. While some configurations welded in 5 and 15 s did not meet the more conservative Eurocode threshold, particularly for thicker plate stacks, almost all configurations exceeded the AWS D8.1M minimum. These results confirm the feasibility of P-FSSW for automotive and structural applications; however, it must be acknowledged that compliance strongly depends many times on the use of long dwell times (15–30 s). Such dwell times may reduce process productivity and therefore may not be practical in industrial applications without further process optimisation. Future work should therefore focus on reducing dwell times while maintaining compliance with the standard requirements.

Author Contributions: Conceptualization, D.G.A., C.L. and D.M.R.; methodology, D.G.A., S.S., C.L. and D.M.R.; formal analysis, D.G.A. and D.M.R.; investigation, D.G.A. and S.S.; resources, C.L. and D.M.R.; writing—original draft preparation, D.G.A. and D.M.R.; writing—review and editing, D.G.A. and D.M.R.; supervision, D.M.R.; funding acquisition, C.L. and D.M.R. All authors have read and agreed to the published version of the manuscript.

Funding: This work was partly financed by FCT/MCTES through national funds (PIDDAC) under the R&D Unit Institute for Sustainability and Innovation in Structural Engineering (ISISE), under reference UID/04029/Institute for Sustainability and Innovation in Structural Engineering (ISISE), by the Centre for Mechanical Engineering, Materials and Processes (CEMMPRE) FCT/MCTES R&D Unit (UIDB/00285/2020) and under the Associate Laboratory Advanced Production and Intelligent Systems ARISE under reference LA/P/0112/2020.

Data Availability Statement: The raw data supporting the conclusions of this article will be made available by the authors on request.

Conflicts of Interest: The authors declare no conflicts of interest.

References

1. Ouisse, M.; Cogan, S. Robust Design of Spot Welds in Automotive Structures: A Decision-Making Methodology. *Mech. Syst. Signal Process.* **2010**, *24*, 1172–1190. [CrossRef]
2. Dubina, D.; Ungureanu, V.; Gîlia, L. Experimental Investigations of Cold-Formed Steel Beams of Corrugated Web and Built-up Section for Flanges. *Thin-Walled Struct.* **2015**, *90*, 159–170. [CrossRef]
3. Naik, B.; Madhavan, M. Comparative Experimental Studies on Stiffened and Unstiffened Flange Cold Formed Steel Welded Sections Using Cold Metal Transfer Welding. *Structures* **2024**, *62*, 106140. [CrossRef]
4. Ungureanu, V.; Both, I.; Burca, M.; Radu, B.; Neagu, C.; Dubina, D. Experimental and Numerical Investigations on Built-up Cold-Formed Steel Beams Using Resistance Spot Welding. *Thin-Walled Struct.* **2021**, *161*, 107456. [CrossRef]
5. *EN 1993-1-3:2006+A1:2014*; CEN, Eurocode 3: Design of Steel Structures—Part 1–3: General Rules—Supplementary Rules for Cold-Formed Members and Sheeting. European Committee for Standardization: Brussels, Belgium, 2014.
6. Pouranvari, M.; Marashi, S.P.H. Critical Review of Automotive Steels Spot Welding: Process, Structure and Properties. *Sci. Technol. Weld. Join.* **2013**, *18*, 361–403. [CrossRef]
7. Rajarajan, C.; Sivaraj, P.; Sonar, T.; Raja, S.; Mathiazhagan, N. Resistance Spot Welding of Advanced High Strength Steel for Fabrication of Thin-Walled Automotive Structural Frames. *Forces Mech.* **2022**, *7*, 100084. [CrossRef]
8. Oikawa, H.; Murayama, G.; Sakiyama, T.; Takahashi, Y.; Ishikawa, T. Resistance Spot Weldability of High Strength Steel (HSS) Sheets for Automobiles. *Nippon Steel Tech. Rep.* **2007**, *95*, 39–45.

9. Janardhan, G.; Mukhopadhyay, G.; Dutta, K. Failure Behaviour of Spot-Welds on Automotive Steel Sheets. *Mater. Today Proc.* **2022**, *62*, 6120–6124. [CrossRef]
10. Wan, X.; Wang, Y.; Fang, C. Welding Defects Occurrence and Their Effects on Weld Quality in Resistance Spot Welding of Ahss Steel. *ISIJ Int.* **2014**, *54*, 1883–1889. [CrossRef]
11. Feng, Z.; Santella, M.L.; David, S.A.; Steel, R.J.; Packer, S.M.; Pan, T.; Kuo, M.; Bhatnagar, R.S. Friction Stir Spot Welding of Advanced High-Strength Steels—A Feasibility Study. *SAE Trans.* **2005**, *114*, 592–598.
12. Ohashi, R.; Fujimoto, M.; Mironov, S.; Sato, Y.S.; Kokawa, H. Effect of Contamination on Microstructure in Friction Stir Spot Welded DP590 Steel. *Sci. Technol. Weld. Join.* **2009**, *14*, 221–227. [CrossRef]
13. Miles, M.P.; Nelson, T.W.; Steel, R.; Olsen, E.; Gallagher, M. Effect of Friction Stir Welding Conditions on Properties and Microstructures of High Strength Automotive Steel. *Sci. Technol. Weld. Join.* **2009**, *14*, 228–232. [CrossRef]
14. Ohashi, R. Study on Friction Stir Spot Welding of Dual-Phase High-Strength Steel Sheets. *Riv. Ital. Della Saldatura* **2011**, *63*, 837–847.
15. Khan, M.I.; Kuntz, M.L.; Su, P.; Gerlich, A.; North, T.; Zhou, Y. Resistance and Friction Stir Spot Welding of DP600: A Comparative Study. *Sci. Technol. Weld. Join.* **2007**, *12*, 175–182. [CrossRef]
16. Xie, G.M.; Cui, H.B.; Luo, Z.A.; Yu, W.; Ma, J.; Wang, G.D. Effect of Rotation Rate on Microstructure and Mechanical Properties of Friction Stir Spot Welded DP780 Steel. *J. Mater. Sci. Technol.* **2016**, *32*, 326–332. [CrossRef]
17. Santella, M.; Hovanski, Y.; Frederick, A.; Grant, G.; Dahl, M. Friction Stir Spot Welding of DP780 Carbon Steel. *Sci. Technol. Weld. Join.* **2010**, *15*, 271–278. [CrossRef]
18. Saunders, N.; Miles, M.; Hartman, T.; Hovanski, Y.; Hong, S.T.; Steel, R. Joint Strength in High Speed Friction Stir Spot Welded DP 980 Steel. *Int. J. Precis. Eng. Manuf.* **2014**, *15*, 841–848. [CrossRef]
19. Miles, M.P.; Ridges, C.S.; Hovanski, Y.; Peterson, J.; Santella, M.L.; Steel, R. Impact of Tool Wear on Joint Strength in Friction Stir Spot Welding of DP 980 Steel. *Sci. Technol. Weld. Join.* **2011**, *16*, 642–647. [CrossRef]
20. Hartman, T.; Miles, M.P.; Hong, S.T.; Steel, R.; Kelly, S. Effect of PCBN Tool Grade on Joint Strength and Tool Life in Friction Stir Spot Welded DP 980 Steel. *Wear* **2015**, *328–329*, 531–536. [CrossRef]
21. Das, H.; Mondal, M.; Hong, S.-T.; Lim, Y.; Lee, K.-J. Comparison of Microstructural and Mechanical Properties of Friction Stir Spot Welded Ultra-High Strength Dual Phase and Complex Phase Steels. *Mater. Charact.* **2018**, *139*, 428–436. [CrossRef]
22. Ebrahimpour, A.; Mostafapour, A.; Nakhaei, M.R. Application of Response Surface Methodology for Weld Strength Prediction in FSSWed TRIP Steel Joints. *Weld. World* **2021**, *65*, 183–198. [CrossRef]
23. Ebrahimpour, A.; Mostafapour, A.; Samadian, K. Finite Element and Experimental Investigation on the Effects of Temperature, Strain and Strain Rate on Microstructure and Mechanical Properties of FSSWed TRIP Steel Joints. *Mater. Res. Express* **2019**, *6*, 16559. [CrossRef]
24. Mazzaferro, C.C.P.P.; Rosendo, T.S.; Tier, M.A.D.D.; Mazzaferro, J.A.E.E.; Dos Santos, J.F.; Strohaecker, T.R. Microstructural and Mechanical Observations of Galvanized TRIP Steel after Friction Stir Spot Welding. *Mater. Manuf. Process.* **2015**, *30*, 1090–1103. [CrossRef]
25. Lomholt, T.C.; Adachi, Y.; Peterson, J.; Steel, R.; Pantleon, K.; Somers, M.A.J. Microstructure Characterization of Friction Stir Spot Welded TRIP Steel. *Adv. Mater. Res.* **2012**, *409*, 275–280. [CrossRef]
26. Dancette, S.; Fabrègue, D.; Massardier, V.; Merlin, J.; Dupuy, T.; Bouzekri, M. Investigation of the Tensile Shear Fracture of Advanced High Strength Steel Spot Welds. *Eng. Fail. Anal.* **2012**, *25*, 112–122. [CrossRef]
27. Lakshminarayanan, A.K.; Annamalai, V.E.; Elangovan, K. Identification of Optimum Friction Stir Spot Welding Process Parameters Controlling the Properties of Low Carbon Automotive Steel Joints. *J. Mater. Res. Technol.* **2015**, *4*, 262–272. [CrossRef]
28. Baek, S.W.; Choi, D.H.; Lee, C.Y.; Ahn, B.W.; Yeon, Y.M.; Song, K.; Jung, S.B. Structure-Properties Relations in Friction Stir Spot Welded Low Carbon Steel Sheets for Light Weight Automobile Body. *Mater. Trans.* **2010**, *51*, 399–403. [CrossRef]
29. Sun, Y.F.; Shen, J.M.; Morisada, Y.; Fujii, H. Spot Friction Stir Welding of Low Carbon Steel Plates Preheated by High Frequency Induction. *Mater. Des.* **2014**, *54*, 450–457. [CrossRef]
30. Hovanski, Y.; Santella, M.L.; Grant, G.J. Friction Stir Spot Welding of Hot-Stamped Boron Steel. *Scr. Mater.* **2007**, *57*, 873–876. [CrossRef]
31. Zou, Y.; Li, W.; Shen, Z.; Su, Y.; Yang, X. Refill Friction Stir Spot Welding of Aluminum Alloys: State-of-the-Art and Perspectives. *Weld World.* **2023**, *67*, 1853–1885. [CrossRef]
32. Tier, M.D.; Rosendo, T.S.; Dos Santos, J.F.; Huber, N.; Mazzaferro, J.A.; Mazzaferro, C.P.; Strohaecker, T.R. The Influence of Refill FSSW Parameters on the Microstructure and Shear Strength of 5042 Aluminium Welds. *J. Mater. Process. Technol.* **2013**, *213*, 997–1005. [CrossRef]
33. Boldsaikhan, E.; Fukada, S.; Fujimoto, M.; Kamimuki, K.; Okada, H. Refill Friction Stir Spot Welding of Surface-Treated Aerospace Aluminum Alloys with Faying-Surface Sealant. *J. Manuf. Process.* **2019**, *42*, 113–120. [CrossRef]
34. Sarkar, R.; Sengupta, S.; Pal, T.K.; Shome, M. Microstructure and Mechanical Properties of Friction Stir Spot-Welded IF/DP Dissimilar Steel Joints. *Metall. Mater. Trans. A Phys. Metall. Mater. Sci.* **2015**, *46*, 5182–5200. [CrossRef]

35. Choi, D.H.; Lee, C.Y.; Ahn, B.W.; Choi, J.H.; Yeon, Y.M.; Song, K.; Park, H.S.; Kim, Y.J.; Yoo, C.D.; Jung, S.B. Frictional Wear Evaluation of WC-Co Alloy Tool in Friction Stir Spot Welding of Low Carbon Steel Plates. *Int. J. Refract. Met. Hard Mater.* **2009**, *27*, 931–936. [CrossRef]
36. Hsieh, M.J.; Chiou, Y.C.; Lee, R.T. Friction Stir Spot Welding of Low-Carbon Steel Using an Assembly-Embedded Rod Tool. *J. Mater. Process. Technol.* **2015**, *224*, 149–155. [CrossRef]
37. Lunetto, V.; De Maddis, M.; Russo Spena, P. Pre-Hole Friction Stir Spot Welding of Dual-Phase Steels and Comparison with Resistance Spot Welding, Conventional and Pinless Friction Stir Spot Welding. *Int. J. Adv. Manuf. Technol.* **2023**, *129*, 2333–2349. [CrossRef]
38. Bakavos, D.; Prangnell, P.B. Effect of Reduced or Zero Pin Length and Anvil Insulation on Friction Stir Spot Welding Thin Gauge 6111 Automotive Sheet. *Sci. Technol. Weld. Join.* **2009**, *14*, 443–456. [CrossRef]
39. Tozaki, Y.; Uematsu, Y.; Tokaji, K. A Newly Developed Tool without Probe for Friction Stir Spot Welding and Its Performance. *J. Mater. Process. Technol.* **2010**, *210*, 844–851. [CrossRef]
40. De Leon, M.; Shin, H.S. Material Flow Behaviours during Friction Stir Spot Welding of Lightweight Alloys Using Pin and Pinless Tools. *Sci. Technol. Weld. Join.* **2016**, *21*, 140–146. [CrossRef]
41. Li, W.; Li, J.; Zhang, Z.; Gao, D.; Wang, W.; Dong, C. Improving Mechanical Properties of Pinless Friction Stir Spot Welded Joints by Eliminating Hook Defect. *Mater. Des.* **2014**, *62*, 247–254. [CrossRef]
42. Yazdi, S.R.; Beidokhti, B.; Haddad-Sabzevar, M. Pinless Tool for FSSW of AA 6061-T6 Aluminum Alloy. *J. Mater. Process. Technol.* **2019**, *267*, 44–51. [CrossRef]
43. Bakavos, D.; Chen, Y.; Babout, L.; Prangnell, P. Material Interactions in a Novel Pinless Tool Approach to Friction Stir Spot Welding Thin Aluminum Sheet. *Metall. Mater. Trans. A Phys. Metall. Mater. Sci.* **2011**, *42*, 1266–1282. [CrossRef]
44. Cao, J.; Zhang, J.; Xing, Y.; Yang, F.; Zhang, X.; Xia, P.; Ma, X. Experimental and Numerical Investigation of a Novel Pinless Friction Stir Spot Welding for Al 1060 Sheets. *Int. J. Adv. Manuf. Technol.* **2024**, *134*, 2537–2546. [CrossRef]
45. Sen, M.; Puri, A.B. An Experimental Investigation on Micro-Friction Stir Welding (MFSW) Process Using Pinless Tool. *J. Mater. Eng. Perform.* **2025**, *34*, 19652–19663. [CrossRef]
46. Aota, K.; Ikeuchi, K. Development of Friction Stir Spot Welding Using Rotating Tool without Probe and Its Application to Low-Carbon Steel Plates. *Weld. Int.* **2009**, *23*, 572–580. [CrossRef]
47. Sun, Y.F.; Fujii, H.; Takaki, N.; Okitsu, Y. Microstructure and Mechanical Properties of Mild Steel Joints Prepared by a Flat Friction Stir Spot Welding Technique. *Mater. Des.* **2012**, *37*, 384–392. [CrossRef]
48. Mousavizade, S.M.; Pouranvari, M. Projection Friction Stir Spot Welding: A Pathway to Produce Strong Keyhole-Free Welds. *Sci. Technol. Weld. Join.* **2019**, *24*, 256–262. [CrossRef]
49. Sun, Y.F.; Fujii, H.; Sato, Y.; Morisada, Y. Friction Stir Spot Welding of SPCC Low Carbon Steel Plates at Extremely Low Welding Temperature. *J. Mater. Sci. Technol.* **2019**, *35*, 733–741. [CrossRef]
50. Alaeibehmand, S.; Ranjbarnodeh, E.; Mirsalehi, S.E. Phase Formation in Pinless Friction Stir Spot Welding of DP600 Dual-Phase Steel to 6061 Aluminum Alloy Dissimilar Joints. *Mater. Charact.* **2025**, *227*, 115268. [CrossRef]
51. Torabi, K.; Beygi, R.; Alikhani, A.; Marques, E.A.S.; Khalfallah, A.; da Silva, L.F.M. Study on Friction Stir Diffusion Bonding of Aluminum to Zinc-Coated Steel: A Comparison to Weld-Brazing. Mater. *Today Commun.* **2025**, *43*, 111833. [CrossRef]
52. Shen, Z.; Ding, Y.; Gerlich, A.P. Advances in Friction Stir Spot Welding. *Crit. Rev. Solid State Mater. Sci.* **2020**, *45*, 457–534. [CrossRef]
53. Akbari, M.; DebRoy, T.; Asadi, P.; Sadowski, T. Recent Advances in Friction Stir Welding/Processing Tools. *J. Manuf. Process.* **2025**, *142*, 99–156. [CrossRef]
54. Andrade, D.G.; Sabari, S.S.; Leitão, C.; Rodrigues, D.M. Influence of the Galvanized Coating Thickness and Process Parameters on Heat Generation and Strength of Steel Spot Welds. *Thin-Walled Struct.* **2021**, *160*, 107401. [CrossRef]
55. Luo, X.; Ren, J.; Li, D.; Qin, Y.; Xu, P. Macro Characteristics of Dissimilar High Strength Steel Resistance Spot Welding Joint. *Int. J. Adv. Manuf. Technol.* **2016**, *87*, 1105–1113. [CrossRef]
56. Liang, J.; Zhang, H.; Qiu, X.; Shi, Y. Characteristics of the Resistance Spot Welding Joints in Dissimilar Thickness Dual-Phase Steels. *ISIJ Int.* **2015**, *55*, 2002–2007. [CrossRef]
57. Zhang, H.; Wei, A.; Qiu, X.; Chen, J. Microstructure and Mechanical Properties of Resistance Spot Welded Dissimilar Thickness DP780/DP600 Dual-Phase Steel Joints. *Mater. Des.* **2014**, *54*, 443–449. [CrossRef]
58. Zhang, H.; Qiu, X.; Xing, F.; Bai, J.; Chen, J. Failure Analysis of Dissimilar Thickness Resistance Spot Welded Joints in Dual-Phase Steels during Tensile Shear Test. *Mater. Des.* **2014**, *55*, 366–372. [CrossRef]
59. Zhang, H.; Qiu, X.; Bai, Y.; Xing, F.; Yu, H.; Shi, Y. Resistance Spot Welding Macro Characteristics of the Dissimilar Thickness Dual Phase Steels. *Mater. Des.* **2014**, *63*, 151–158. [CrossRef]
60. *AWS D8.1M*; Specification for Automotive Weld Quality-Resistance Spot Welding of Steel. AWS: Doral, FL, USA, 2021.
61. Andrade, D.G.; Leitão, C.; Rodrigues, D.M. Influence of Base Material Characteristics and Process Parameters on Frictional Heat Generation during Friction Stir Spot Welding of Steels. *J. Manuf. Process.* **2019**, *43*, 98–104. [CrossRef]

62. Chen, Y.; Zhang, D.; Liu, Y.; Li, H.; Xu, D. Effect of Dissolution and Precipitation of Nb on the Formation of Acicular Ferrite/Bainite Ferrite in Low-Carbon HSLA Steels. *Mater. Charact.* **2013**, *84*, 232–239. [CrossRef]
63. Webel, J.; Herges, A.; Britz, D.; Detemple, E.; Flaxa, V.; Mohrbacher, H.; Mücklich, F. Tracing Microalloy Precipitation in Nb-Ti HSLA Steel during Austenite Conditioning. *Metals* **2020**, *10*, 243. [CrossRef]
64. Gong, P.; Palmiere, E.J.; Rainforth, W.M. Dissolution and Precipitation Behaviour in Steels Microalloyed with Niobium during Thermomechanical Processing. *Acta Mater.* **2015**, *97*, 392–403. [CrossRef]
65. Wang, Z.; Wu, J.; Li, J.; Wu, X.; Huang, Y.; Li, X. Effects of Niobium on the Mechanical Properties and Corrosion Behavior of Simulated Weld HAZ of HSLA Steel. *Metall. Mater. Trans. A Phys. Metall. Mater. Sci.* **2018**, *49*, 187–197. [CrossRef]
66. Zurob, H.S.; Brechet, Y.; Purdy, G. A Model for the Competition of Precipitation and Recrystallization in Deformed Austenite. *Acta Mater.* **2001**, *49*, 4183–4190. [CrossRef]